JGR Space Physics

Key Points:
- Significant energy conversion and dissipation occurred around the separatrices within the IDR
- The thickness of the electron isotropic region within the IDR strongly depends on the horizontal distance to the X line
- The normal electric field and energy dissipation show evident asymmetry with respect to the neutral sheet

Correspondence to:
M. Zhou,
mengzhou@ncu.edu.cn

Sub-ion-scale Dynamics of the Ion Diffusion Region in the Magnetotail: MMS Observations

M. Zhou[1,2], **H. Y. Man[1,3]**, **Z. H. Zhong[1,4]**, **X. H. Deng[1,4]**, **Y. Pang[1]**, **S. Y. Huang[5]**, **Y. Khotyaintsev[6]**, **C. T. Russell[7]**, and **B. Giles[8]**

[1]Institute of Space Science and Technology, Nanchang University, Nanchang, China, [2]State Key Laboratory of Space Weather, National Space Science Center, Chinese Academy of Sciences, Beijing, China, [3]Department of Physics, School of Science, Nanchang University, Nanchang, China, [4]Key Laboratory of Poyang Lake Environment and Resource Utilization, Ministry of Education, School of Resources Environmental & Chemical Engineering, Nanchang University, Nanchang, China, [5]School of Electronic Information, Wuhan University, Wuhan, China, [6]Swedish Institute of Space Physics, Uppsala, Sweden, [7]Department of Earth, Planetary, and Space Sciences, University of California, Los Angeles, CA, USA, [8]Goddard Space Flight Center, NASA, Greenbelt, MD, USA

Abstract This paper reports magnetospheric multiscale (MMS) observations of the sub-ion-scale dynamics within the ion diffusion region (IDR) in the Earth's magnetotail. MMS crossed the IDR from the southern to the northern hemisphere, at about two ion inertial length earthward of the X line with a small guide field. Electrons were anisotropic in the inflow region of the IDR and turned into isotropic within the IDR. The isotropization of the electrons was probably due to the pitch angle scattering in highly curved magnetic field lines. We suggest that the thickness of the electron isotropic region strongly depends on the horizontal distance to the X line. The out-of-plane current bifurcated in the IDR. It peaked at the boundaries between the inflow and outflow electrons around the separatrices. Magnetic energy conversion and dissipation predominantly occurred at the peak of the out-of-plane current instead of at the neutral sheet center where $B_L = 0$. Both the energy dissipation and normal electric field E_N exhibited evident asymmetry with respect to the neutral sheet. The energy dissipation was larger around the northern separatrix than around the southern separatrix. The electric field E_N showed a tripolar variation across the neutral sheet, that is, a unipolar E_N around the southern separatrix and a bipolar E_N around the northern separatrix. The reasons and implications of these asymmetries are discussed.

1. Introduction

It is widely accepted that magnetic reconnection is initiated in a small-scale diffusion region and causes large-scale magnetic topology changes. The core concept of the Hall reconnection model is the two-scale diffusion region based on the different masses of ions and electrons: The ion diffusion region (IDR) and the electron diffusion region (EDR). Ions (electrons) are demagnetized and decoupled from magnetic fields in the IDR (EDR). It has been suggested that Hall effect, resulted from the decoupling of the ion and electron motion in the IDR, is crucial for fast reconnection (e.g., Birn et al., 2001). However, some studies challenge this conclusion by finding that fast reconnection is also achieved in electron-positron plasma, where Hall effect vanishes (Bessho & Bhattacharjee, 2005). Recent development of fast reconnection theory suggests that macroscopic upstream/inflow conditions determine the fast reconnection rate while microphysics within the diffusion region are not important (Liu et al., 2017).

In situ observations of the IDR in the Earth's magnetosphere in the past decade, from Cluster (e.g., Runov, 2003; Borg et al., 2005; Eastwood et al., 2007; Eastwood, Phan, et al., 2010; Wang et al., 2010, 2012; Nakamura et al., 2006; Zhou et al., 2017), Wind (e.g., Øieroset et al., 2001), Geotail (e.g., Deng & Matsumoto, 2001; Nagai et al., 2011), and THEMIS missions (e.g., Teh et al., 2010), have established the quadrupolar out-of-plane Hall magnetic field and bipolar normal Hall electric field in/around the IDR, which are consistent with numerical simulations (Pritchett, 2001). These observations found coherent structures in the IDR, including the secondary magnetic islands and dipolarization fronts (Chen et al., 2008; Fu et al., 2013; Huang et al., 2012; Wang et al., 2010; Zhou et al., 2017). Abundant plasma waves, such as kinetic Alfven waves (Chaston et al., 2005; Huang et al., 2010), lower hybrid drift waves (Zhou et al., 2009; Zhou, Li, et al., 2014), whistler waves (Deng and Mastumoto, 2001; Zhou et al., 2011; Huang et al., 2016, 2017), and
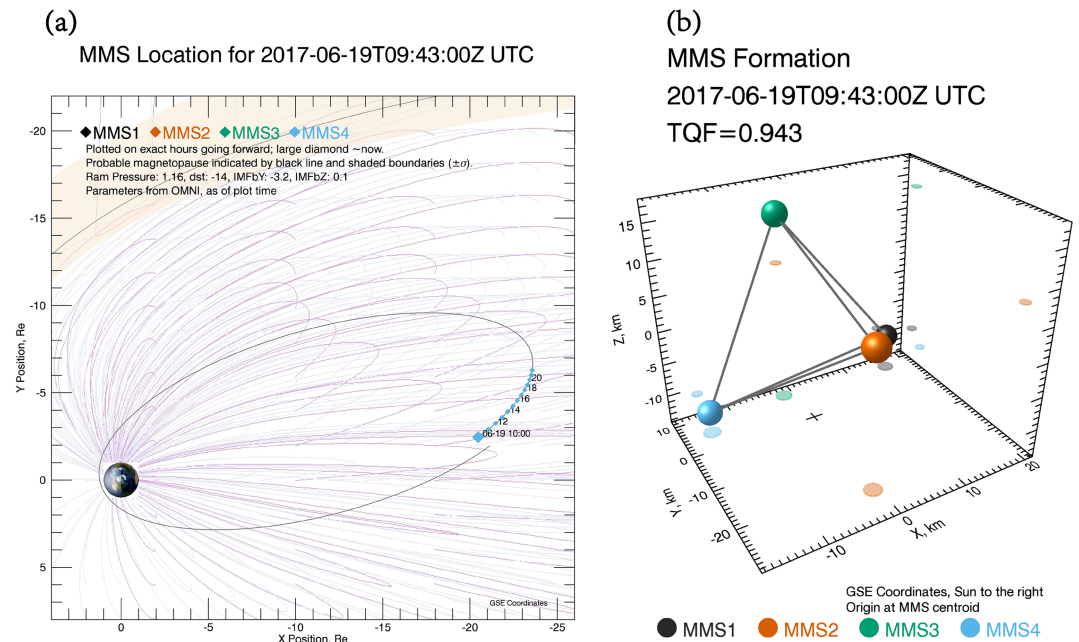
Figure 1. (Panel a) Magnetospheric multiscale (MMS) orbit during the whole day of 19 June 2017 and (panel b) formation of the four spacecraft in space at 09:43 UT. The orbit in panel (a) is in geocentric solar ecliptic (GSE) coordinate system.

high-frequency electrostatic waves (Viberg et al., 2013), have been detected within the IDR. These waves may be important in energy dissipation and transport. They also provide important clues on how the particles are regulated by reconnection. Sub-ion-scale physics and electron dynamics in the IDR have rarely been investigated through these studies, since these missions do not have high-resolution electron data even though they provide sufficient high-resolution electromagnetic field data.

Since 2015, magnetospheric multiscale (MMS) has provided high-resolution measurements of the IDR at the dayside magnetopause (e.g., Graham et al., 2016; Phan et al., 2016; Wang et al., 2016; Zhou et al., 2016). These IDRs were associated with asymmetric reconnection, in which the Hall electromagnetic fields are asymmetric with respect to the reconnecting magnetopause current sheet (Tanaka et al., 2008; Mozer et al., 2008; Dai, 2018). Zhou et al. (2016) studied high-frequency plasma waves and inferred the wave-particle interactions based on the high-resolution electron velocity distributions. Wang et al. (2016) found the ion demagnetization and energization in the IDR. Graham et al. (2016) found the electron heating and intense electron currents due to lower hybrid drift waves. Phan et al. (2016) also reported intense electron currents within the IDR and suggested that sub-ion-scale process is important in the IDR.

MMS started phase 2b in the magnetotail from May 2017. Two EDRs, which were associated with symmetric reconnection in the magnetotail, have already been reported in detail (Torbert et al., 2018; Zhou et al., 2019). However, there is lack of detailed analysis of the IDR in symmetric reconnection from MMS. In this paper, we reveal the fine structures of the IDR by MMS observations in the magnetotail. The data from the following instruments onboard MMS have been used in this study: the fluxgate magnetometer (Russell et al., 2016), the fast plasma instrument (FPI; Pollock et al., 2016), and the electric double probe (Ergun et al., 2016; Lindqvist et al., 2016).

The remainder of this paper is organized as follows. We demonstrate the global context of this event in section 2. The observations of the IDR are depicted in section 3. Section 4 shows the characteristics of this IDR. Discussion and summary are given in section 5.

2. Overview of the X line in the Magnetotail

MMS was around $[-20.4, -2.5, 2.8]$ R_E in the geocentric solar ecliptic coordinate system in the magnetotail at 09:43 UT (Figure 1a). Figure 1b shows that MMS constituted a nearly perfect tetrahedron in space with
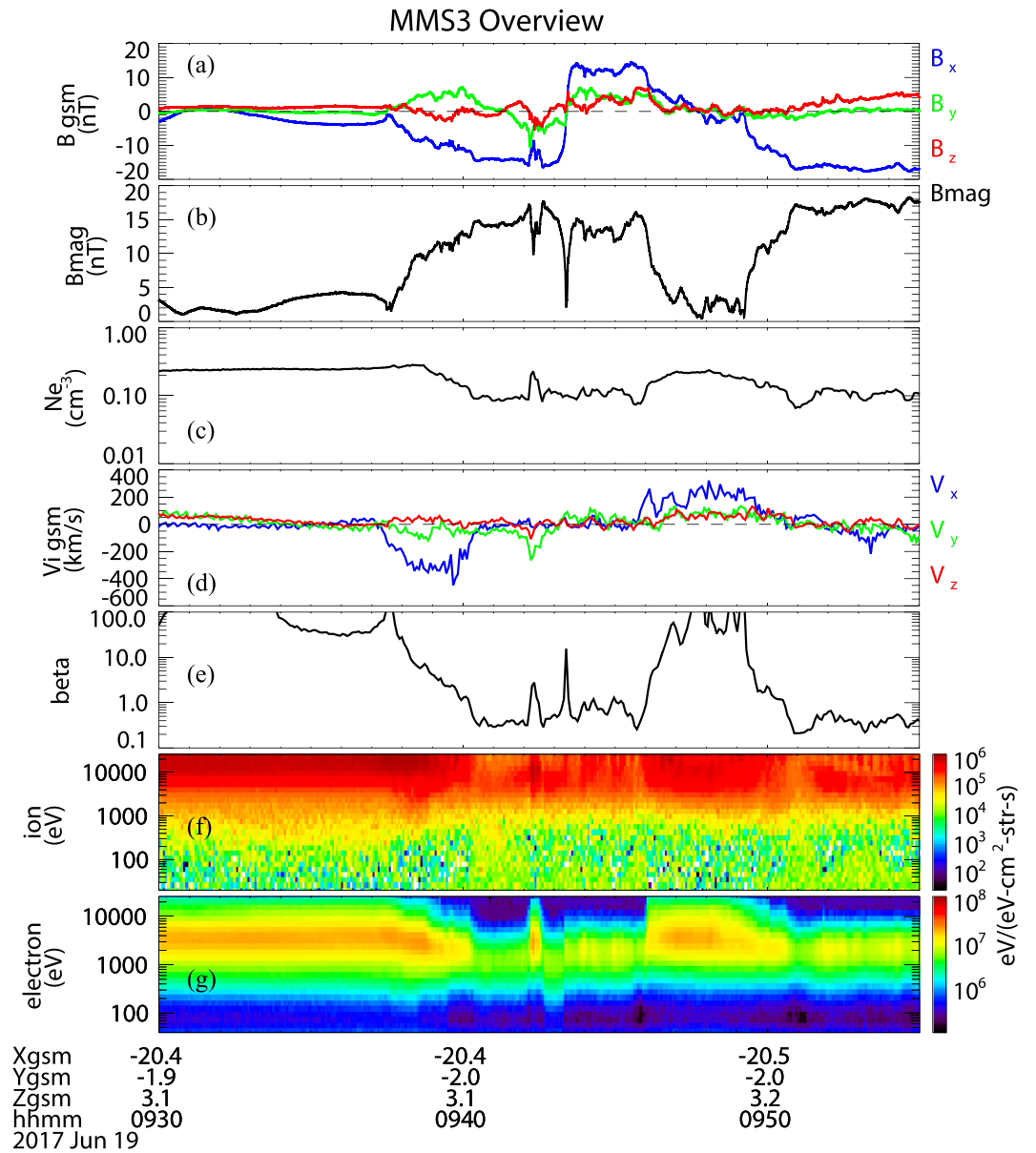
Figure 2. Overview of MMS3 observations from 09:30 to 09:55 UT. From the top to the bottom are (a) three components of the magnetic field; (b) total magnetic field; (c) plasma number density; (d) ion bulk velocities; (e) ion plasma β; and (f) ion and (g) electron omnidirectional differential energy flux. Vectors are presented in geocentric solar magnetospheric (GSM) coordinate system. MMS, magnetospheric multiscale.

tetrahedron quality factor of 0.943 at 09:43 UT (Robert & Roux, 1993). The average spacing of the four spacecraft was 24 km ~ 0.033 d_i ~ 1.5 d_e, where d_i ~ 720 km is the ion inertial length and d_e ~ 16 km is the electron inertial length based on plasma number density of 0.1/cm^3.

Figure 2 displays the MMS3 observations from 09:30 to 09:55 UT. The vectors are presented in the geocentric solar magnetospheric (GSM) coordinate system. The spacecraft detected a tailward (~−400 km/s) to earthward (~200 km/s) ion bulk flow reversal. The flow reversal was accompanied by the polarity change of magnetic field B_z from negative to positive, suggesting that a tailward retreating X line passed the spacecraft. There was a flow quiescent period between the tailward and the earthward flow. We should note that the flow speed is underestimated since a significant number of ions were above the upper energy limit of the FPI, as is shown in Figure 2f. The plasma density was relatively stable (~0.1 cm^{-3}) during the X line crossing and was slightly higher in the ambient quiet plasma sheet (~0.2 cm^{-3}).

MMS was deep in the plasma sheet, where ion plasma β exceeded 10 and magnetic field B_x was around zero, during 09:30–09:36 UT, before the onset of the tailward flow. MMS moved southward at 09:37 UT as it detected the enhancement of the tailward flow, which marks the onset of a reconnection earthward of the spacecraft. MMS exited the flow channel after 09:41 UT when β_i observed by MMS was below 0.5. Then, MMS encountered a bulge or a flux rope in the southern hemisphere approximately from 09:41:30 to 09:42:30 UT, when it recorded a bipolar variation of B_z. MMS was engulfed into the central plasma sheet as it observed the elevated β_i up to 3 and the enhancement of the ion/electron energy fluxes above 1 keV. A dawnward ion flow was in association with the flux rope or the bulge. MMS then crossed the neutral sheet rapidly from the southern to the northern hemisphere at around 09:43 UT, during the quiescent flow interval.

The earthward flow started at about 09:46 UT when MMS approached the neutral sheet again. It persisted nearly 5 min and reversed sign when MMS exited the neutral sheet. Figure 6a depicts the trajectory of MMS through this X line from the tailward to the earthward side. MMS was in the plasma sheet (plasma β_i was around 0.5) when it did not observe the high-speed outflow during 09:42:30–09:43 UT and 09:44–09:45 UT. This implies that the reconnection did not reach the lobe, that is, it occurred in closed field lines.

3. Observations of the IDR

In the following, we focus on the neutral sheet crossing during the flow reversal. We have transferred the vectors into an LMN coordinate system, which was obtained by applying the minimum variance analysis on the magnetic field between 09:43:09 and 09:43:34 UT (Sonnerup & Scheible, 1998). The rotation matrix from GSM to LMN is: $\mathbf{L} = [0.958, 0.272, 0.096]$, $\mathbf{M} = [-0.254, 0.640, 0.725]$ and $\mathbf{N} = [0.136, -0.718, 0.682]$. Here, $\mathbf{L}$ corresponds to the maximum eigenvalue and points to the reconnecting component, $\mathbf{N}$ corresponds to the minimum eigenvalue and points to the normal of the neutral sheet, and $\mathbf{M}$ corresponds to the intermediate eigenvalue and completes the right-handed orthogonal coordinate system, that is, $\mathbf{M} = \mathbf{N} \times \mathbf{L}$. The ratio between the intermediate and the minimum eigenvalue is 22. The derived $\mathbf{N}$ has been double checked by timing analysis, which provides the moving speed of the neutral sheet in the normal direction $V_N \sim -90$ km/s. The two vectors are only 8° different between each other, indicating that the obtained normal is reliable. We note that the neutral sheet normal deviated significantly from Z_{gsm}, which is a common feature of magnetotail current sheets and was likely caused by the kink-type or sausage-type instability or other fluid instabilities (Sharma et al., 2008 and references therein).

Figure 3 shows the MMS3 burst mode observations of this neutral sheet between 09:43:17 and 09:43:33 UT. MMS crossed the neutral sheet on the earthward side of this X line, because both the ion flow V_{iL} and electron flow V_{eL} together with the magnetic field B_N were positive throughout this interval. There was an enhancement of V_{iL} (~200 km/s) in the neutral sheet in comparison to the inflow region. Note again that V_{iL} is underestimated due to the limited energy coverage of FPI. V_{iL} was smaller than the ion outflow speed observed at around 09:39 and 09:48 UT. It was also smaller than the electron outflow V_{eL}, which means that MMS was close to the X line as the ions had not been accelerated to the speed in the exhaust further away from the X line. Note that the ion outflow speed is generally smaller than the inflow Alfven speed (Wu and Shay, 2011). In this event, the inflow Alfven speed $V_{A,in}$ was about 1000 km/s based on the inflow magnetic field ~15 nT and plasma density ~0.1/cm^3.

The reverse of B_L was accompanied by a bipolar variation of the out-of-plane magnetic field B_M from negative to positive. The bipolar variation is superposed on a small guide field $B_g \sim 1.5$ nT ~ 0.1 B_0, which is inferred from the shear angle (~170°) between the two asymptotic magnetic fields at around 09:45:40 and 09:52:10 UT, respectively. The polarity change is consistent with Hall quadrupolar magnetic field (Pritchett, 2001; Eastwood, Phan, et al., 2010). The positive B_M' has a larger magnitude than the negative B_M', here $B_M' = B_M - B_g$.

A Hall current loop in the reconnecting plane (L-N plane) was associated with the Hall magnetic field. It consisted of an outward current in $+\mathbf{L}$ above/below the neutral sheet and an inward current in $-\mathbf{L}$ bounded by the two outward currents (Figures 3f and 3g). The current densities calculated by the curlometer technique (Figure 3f) and from the plasma moments (Figure 3g) are similar, except that the magnitude was larger for the current derived from the plasma moments than from Ampere's law. The Hall current was mainly carried
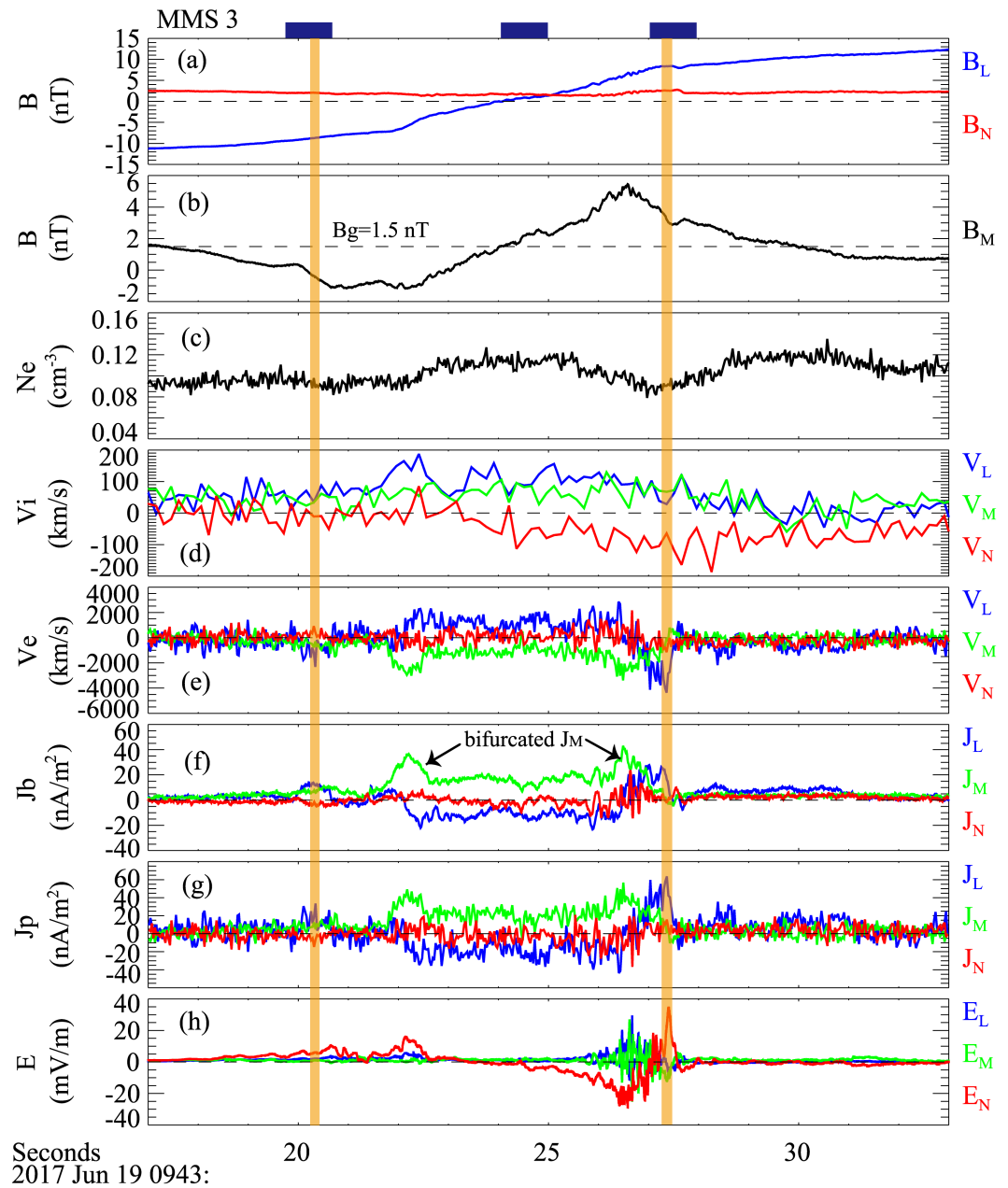
Figure 3. MMS3 burst mode observations of the ion diffusion region. (a) Magnetic fields B_L (black) and B_N (red); (b) magnetic field B_M; (c) electron density; (d) ion bulk velocities; (e) electron bulk velocities; (f) current density calculated by the curlometer technique and (g) by the plasma moments, that is, $J = nq (V_i − V_e)$; and (h) three components of electric field. Vectors are presented in the LMN coordinate system. The orange shadows mark the separatrices. The three blue bars denote the times of the ion velocity distributions shown in Figure 5. MMS, magnetospheric multiscale.

by electrons since the electron velocity was much greater than the ion velocity. This Hall current loop agrees well with simulations (e.g., Lu et al., 2010) and generated the perturbations of B_M. We notice that a current in the +**N** direction is needed to close the Hall current loop at the reversal point of J_L near the northern separatrix. However, we see a −**N**-directed current from the particle data. The closing of this Hall current loop was probably not detected by MMS but at a location closer to the X line. Lu et al. (2010) pointed out that electrons flow toward the X line along the separatrix, while the outflow electrons are at the inner side of the separatrix. The two orange shadows in Figure 3 mark the locations of the two separatrices, which are coincident with the peak speeds of the inflowing electrons. A density dip was observed corresponding to the northern separatrix, while the density did not change obviously around the southern separatrix.

The out-of-plane current J_M bifurcated within the IDR (Figure 3f). This feature is quite common in current sheets in space plasmas. For instance, it has been observed in the magnetotail associated with or without reconnection signatures (Asano et al., 2003; Nakamura et al., 2006; Runov et al., 2003). The peak J_M was coincident with the reversal of J_L and in the inner side of the two separatrices. The width of J_M was about 90 km ~ 5.3 d_e, thus they were electron-scale current layers.

The normal electric field E_N was positive below the neutral sheet and mostly negative above the neutral sheet (Figure 3h). This is consistent with previous observations showing the convergent electric field around the IDR (Borg et al., 2005; Eastwood, Phan, et al., 2010). The peak magnitude of E_N was about 20 mV/m. Figure 4 presents the measured electric field $\mathbf{E}$, the ion convective electric field $-\mathbf{V}_i \times \mathbf{B}$, and the electron convective electric field $-\mathbf{V}_e \times \mathbf{B}$. It clearly shows that $|\mathbf{E}|$ was much larger than $|-\mathbf{V}_i \times \mathbf{B}|$ for almost the entire interval, that is, the ion frozen-in condition was violated. The normal electric field E_N was mainly balanced by $-\mathbf{V}_e \times B$, that is, E_N was mainly the Hall electric field $J \times B/n_e e = V_i \times B - V_e \times B \sim -V_e \times B$ given that quasi-neutrality ($n_i \approx n_e$) was satisfied. From the perspective of the ion momentum equation, the Hall electric field was mainly balanced by ion pressure gradient term (Dai et al., 2015, 2017; Zhang et al., 2017). Note that there was a positive E_N peak adjacent to the negative E_N above the neutral sheet. This additional positive E_N will be discussed in the next section. The structured electromagnetic perturbations, that is, the bipolar B_M variation and E_N variation between the two orange shadows in Figure 3, were also suggested as the manifestation of kinetic Alfven waves (Dai et al., 2017). Here, $E_N \sim 30$ mV/m and $B_M \sim 3.5$ nT, thus the ratio E_N/B_M is around 860 km/s, which is close to the Alfven speed. This supports the kinetic Alfven wave explanation of the Hall fields.

The ion velocity distributions during this crossing are displayed in Figure 5. Figures 5a and 5c present the distributions around the two separatrices, while Figure 5b shows the distribution in the neutral sheet. The three corresponding times are indicated by the blue bars in Figure 3. Figure 5b shows the counter-streaming ions (marked by the two circles in the V_M-V_N plane) along the normal of the neutral sheet in the central current sheet. The peak velocities were around 500 km/s. These were meandering ions bounced back and forth across the neutral sheet (Wygant et al., 2005). The distribution slightly shifts toward the $+\mathbf{L}$ direction because of the accelerated outflow along $+\mathbf{L}$. There is a population in $+\mathbf{M}$ around ~1,000 km/s ~ 5 keV (marked by the circle in the V_L-V_M plane). These ions were probably accelerated by the reconnection electric field in the IDR. This speed is substantially larger than the bulk speed of the ions. The ion velocity distributions in V_M-V_N plane (perpendicular to the magnetic field) around the two separatrices exhibit nongyrotropy, which is more evident in Figure 5c that the phase space densities on the upper right and lower left quadrants are larger than that in the two other quadrants. The nongyrotropic ion distributions were likely the consequence of the mixture of incoming ions and already accelerated ions (Dai et al., 2015). We can safely conclude that MMS crossed an IDR of this X line based on the evidence of Hall electromagnetic fields, Hall current, and the demagnetized ions. Figure 6b illustrates the MMS trajectory and the geometry of the IDR, including the Hall electromagnetic fields and Hall current.

Based on the well-structured Hall magnetic fields and simple geometry analysis, we estimated the reconnection rate and the distance of the crossing point to the X line in the $\mathbf{L}$ direction. The cone angle was estimated by $\theta = \tan^{-1}|B_N/B_L| \approx 15°$, where B_N and B_L are the averaged values at the two separatrices. This estimation is reliable in a laminar reconnection where separatrix can be clearly identified and B_N and B_L are relatively stable. By using the formula in Liu et al. (2017) and the cone angle, we found the dimensionless reconnection rate was about 0.19, which corresponds to an inflow speed of 200 km/s and 3 mV/m E_M over the mesoscale region just outside the diffusion region. However, the flow speed $|V_N|$ was less than 200 km/s (Figure 3d), and the electric field E_M was less than 3 mV/m in the inflow region. This discrepancy may be due to that the reconnection electric field does not simply map from the microscale to the mesoscale as the model assumes. As the data indicates, this is likely an oversimplification in Liu et al. (2017).

We noticed that the separation between the southern separatrix (the peak speed of the inflow electrons) and $B_L = 0$ is dt1 = 4 s, and the separation is about dt2 = 3 s for the northern separatrix (See Figure 3e). The difference was probably due to the oblique crossing of this IDR by MMS, which resulted in the different vertical distances between the neutral sheet and the two separatrices (see Figure 6b). The distance between the X line and the crosspoint of the MMS trajectory and the neutral sheet is given by $\frac{dt2\delta1+dt1\delta2}{(dt1+dt2)\tan\theta} \sim 1,200$ km ~ 1.6 d_i,
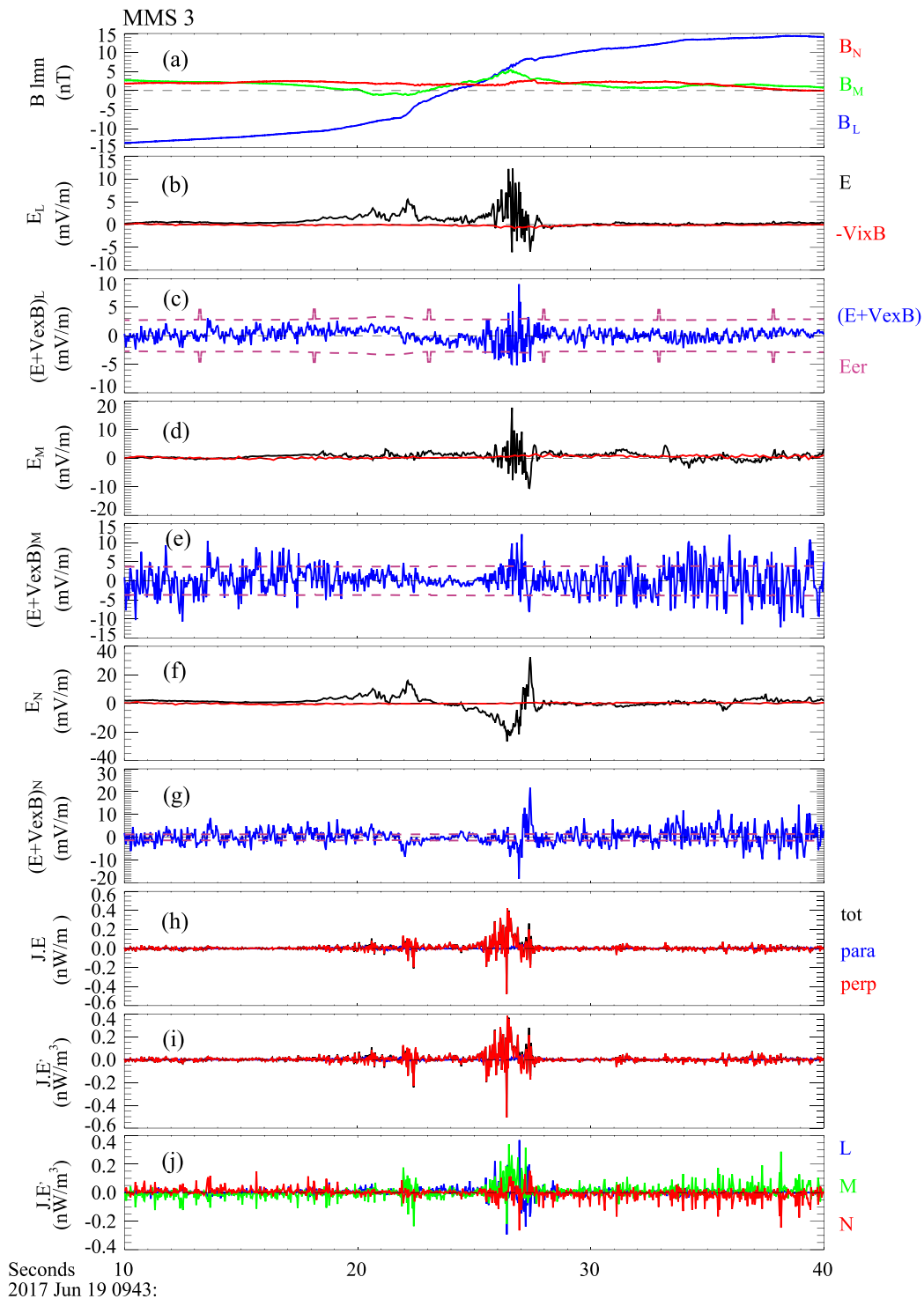
Figure 4. (a) Three components of the magnetic field; panels (b), (d), and (f) show the three components of the electric field, respectively. The black traces denote the measured electric field E, while the red traces denote $-V_i \times B$. Panels (c), (e), and (g) display the three components of electric field in the electron frame $E + V_e \times B$ (blue) and the errors of the measured electric fields (purple), respectively. Panel (i) shows the energy conversion rate $J \cdot E$, and panel (j) shows the energy dissipation rate $J \cdot E'$. The red traces in panels (h) and (i) denote the contribution from the perpendicular electric field, while the blue traces denote the contribution from the parallel electric field. Panel (j) presents $J_L E_L'$ (blue), $J_M E_M'$ (green), and $J_N E_N'$ (red). The periodic peaks of the error bars in panel (c) are related to the shadowing of the SDP probes by the ADP boom. Here, SDP is the spin-plane double probe instrument, and ADP is the axial double probe instrument. There are four SDP probes, so there are four shadows per spin: 20 s/4 = 5 s. When one of the probes is in shadows, there will be a spike in the electric field. The electric double probe instrument team has a model for this spike and has removed most of it from the data. But there is always something left and therefore using a higher error value at this time.
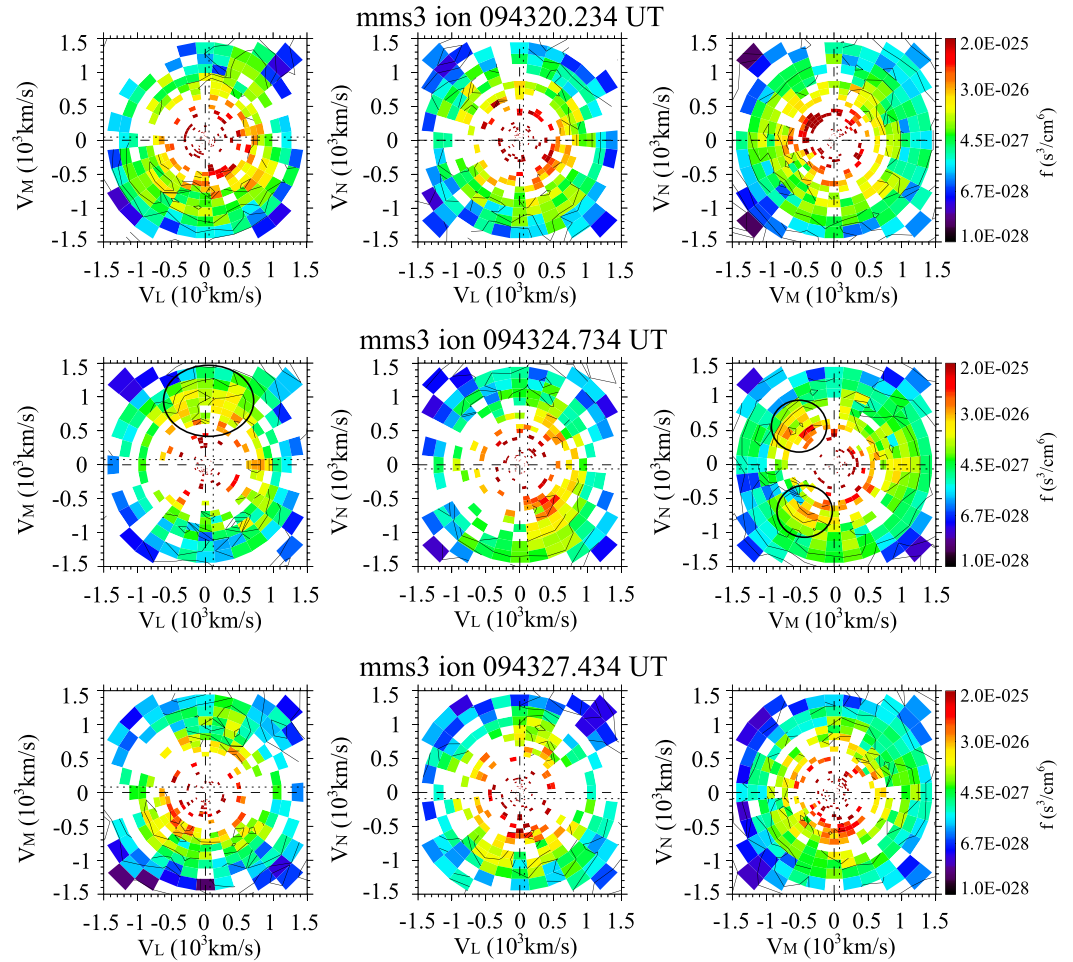
Figure 5. Ion velocity distributions at (a) 09:43:20.234 UT, (b) 09:43:24.734 UT, and (c) 09:43:27.434 UT. The distributions have been averaged in a 0.9-s window with the central time indicated in the title. For each panel, from the left to the right are the distributions in V_L-V_M, V_L-V_N, and V_M-V_N plane, respectively.

where v_N ~90 km/s and $\delta 1 = v_N dt1 (\delta 2 = v_N dt2)$ is the vertical distance between the southern (northern) separatrix and the neutral sheet. This method is similar to that used in Phan et al. (2007) to infer how far the electron jet was from the X line. Furthermore, the motion speed of the X line in the **L** direction is estimated as $\frac{v_N(dt1-dt2)}{\tan\theta(dt1+dt2)}$ ~ 48 km/s. Although the X line moved tailward on average from 09:36 to 09:50 UT, it occasionally moved earthward during this interval as demonstrated here. The lower limit height of this IDR equals the vertical distance between the two separatrices at the crosspoint of MMS trajectory and the southern separatrix, that is, $2\delta 1 \approx 1$ d_i.

4. Novel Properties of the IDR

Figures 4h and 4i show that the energy conversion J·E and dissipation J·E′ within the IDR were mainly at the peak of the current J_M instead of at the current sheet center where $B_L = 0$. Here, E′ is the electric field in the electron rest frame, that is, $E' = E + V_e \times B$. The difference between E and $-V_e \times B$ is larger than the errorbar of the electric field in the regions with significant J·E′, as is shown in Figures 4c, 4e, and 4g. The peak value of J·E′ was about 0.4 nW/m³, which is comparable to those observed in the EDR in the magnetotail (Torbert et al., 2018; Zhou et al., 2019). A Super-Alfvenic electron jet with V_{eL} ~ 2,000 km/s ~ 2 $V_{A,in}$ was observed at $B_L = 0$; however, this electron jet did not correspond to significant energy dissipation because the electrons were mostly frozen-in to the magnetic fields. This contrasts with the energy dissipation in the IDR reported by Zhou et al. (2016). They found the most intense energy dissipation at the center of the IDR.
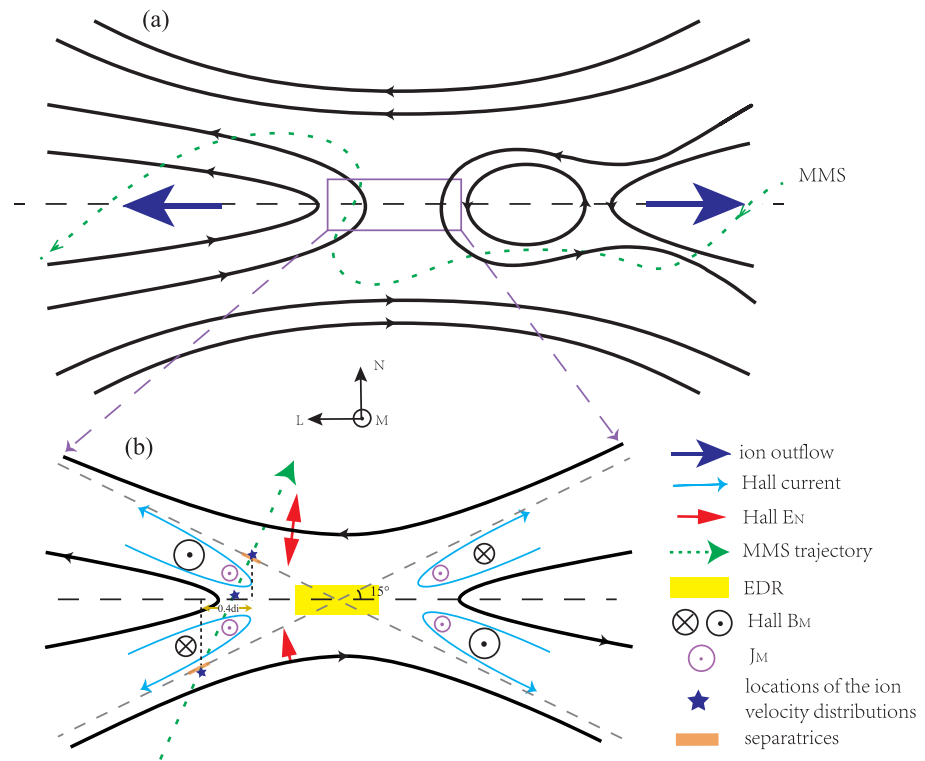
Figure 6. (a) Schematics of the X line and (b) the ion diffusion region (IDR) detected by magnetospheric multiscale (MMS). MMS was initially in the central plasma sheet tailward side of the X line. Then it moved southward and encountered the southern portion of a tailward-moving flux rope or bulge. MMS then moved to the earthward side of this X line and crossed the IDR from the southern to the northern hemisphere. It finally moved southward and crossed the neutral sheet again in the earthward exhaust.

The nonzero $J\cdot E'$ means the existence of nonideal electric field around the separatrices, which has been reported in particle simulation (Zhou et al., 2012). Comparing Figures 4h and 4i, we find that $J\cdot E$ and $J\cdot E'$ were nearly the same, which implies that most of the magnetic energy went to heat instead of bulk accelerating the plasma. $J\cdot E$ and $J\cdot E'$ were mainly contributed by the perpendicular current and electric field, while the work done by the parallel electric field was negligible. Figure 4j decomposes $J\cdot E'$ into $J_L E_L'$, $J_M E_M'$, and $J_N E_N'$. We see that $J_M E_M'$ dominates over the other two components since J_M was larger than the current densities in the other two directions.

One remarkable feature of the energy conversion and dissipation is the asymmetry between the southern and northern hemisphere. Figure 4i clearly shows that the magnitude of $J\cdot E'$ is larger in the northern hemisphere than in the southern hemisphere. The average energy dissipation around the northern separatrix was positive ~0.035 nW/m^3, while it was nearly zero around the southern separatrix.

Another intriguing feature of this IDR is the tripolar Hall E_N structure. It has been found in a recent particle-in-cell simulation with guide field (Fu et al., 2018) but has not been reported experimentally. The polarity change of this tripolar E_N is consistent with the results in Fu et al. (2018), which demonstrates that the bipolar E_N appears in the larger B_M side. However, one major discrepancy is that the positive E_N adjacent to the negative E_N is mainly due to the ion convective electric field in Fu et al. (2018), whereas the positive E_N observed here was much larger than $-V_i \times B$. This positive E_N was also larger than $-V_e \times B$, thus requiring the divergence of electron pressure tensor or the electron inertial to balance it. The duration of this positive E_N was about 0.3 s, hence its spatial scale was about 27 km ~ 2 d_e.

Figure 7 compares $J\cdot E'$ and E_N observed by the four spacecraft. Obvious asymmetry in $J\cdot E'$ and the electric field E_N with respect to the neutral sheet was observed by all the four spacecraft. In particular, $J\cdot E'$ around the southern separatrix was even negative as observed by MMS2. The four spacecraft were separated by
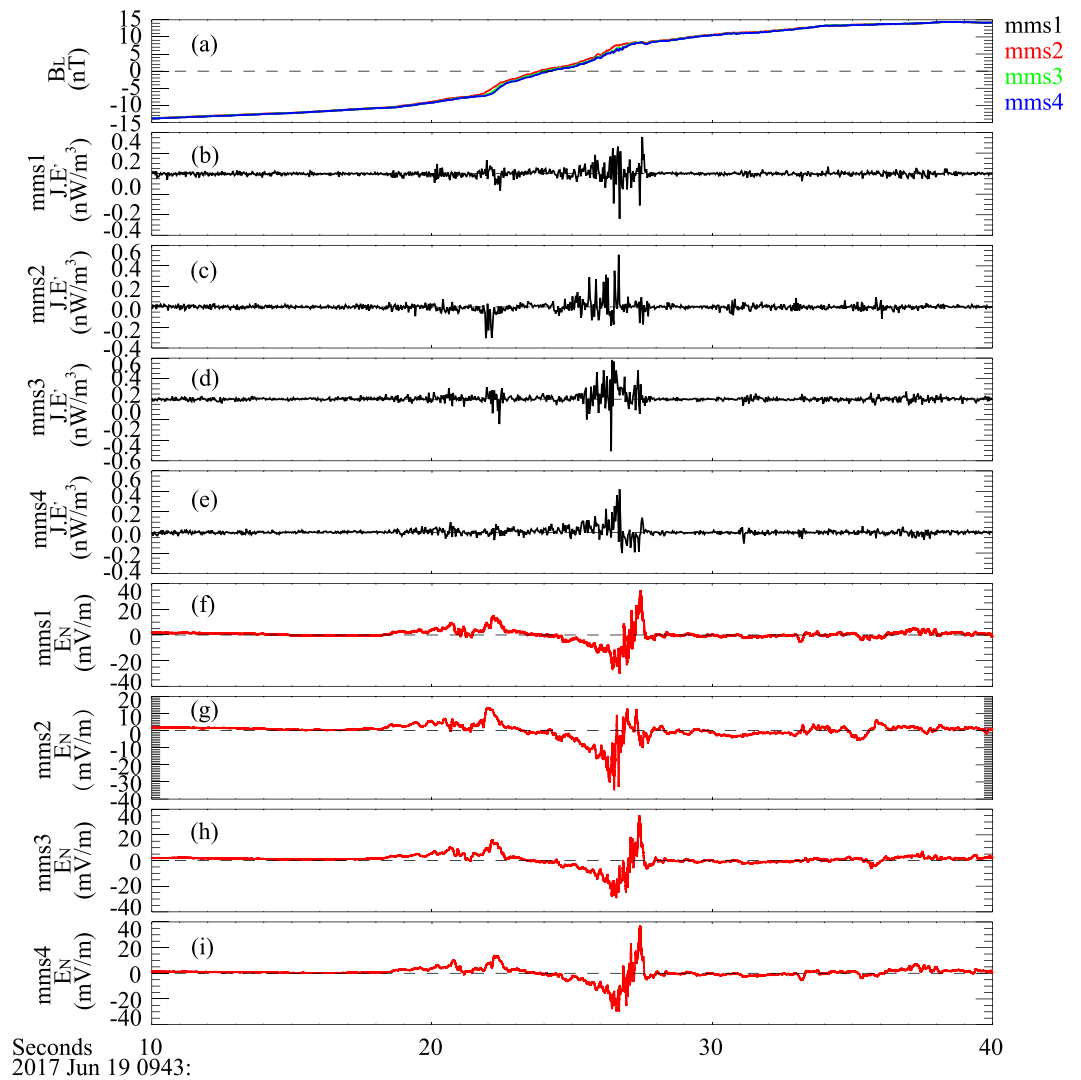
Figure 7. The magnetic field B_L (a), the energy dissipation rate $J \cdot E'$ (b–e), and the electric field E_N (f–i) measured by the four spacecraft.

about one electron inertial length from each other, thus implies the electron-scale variations of $J \cdot E'$ around the separatrix region. E_N observed by the other three spacecraft are similar to that observed by MMS3, except the positive E_N at the northern separatrix observed by MMS2 was relatively smaller. This is consistent with our interpretation that the positive E_N near the northern separatrix was associated with electron-scale physics.

Figure 8 presents the electron temperature and pitch angle distributions around the neutral sheet. Electrons were isotropic further away from the neutral sheet. Significant temperature anisotropy with $T_\parallel > T_\perp$ appeared once $|B_L|$ was less than 12 nT. The parallel temperature anisotropy resulted from the bidirectional electrons in the energy range of 250–700 eV and 800–4,000 eV, which are displayed in Figures 8c and 8d, respectively. The parallel temperature enhanced suddenly around the separatrices and led to a maximum anisotropy $T_\parallel/T_\perp \approx 3$ at the southern separatrix and $T_\parallel/T_\perp \approx 2$ at the northern separatrix. The temperature and electron pitch angle distributions were isotropic in the center of the IDR where $|B_L| < 5$ nT. The thickness of the isotropic region was about 270 km ~ 16 d_e. The average temperature was higher in the isotropic region than in the anisotropic region. We notice that the electron temperature was also asymmetric with respect to the neutral sheet, that is, the temperature on the northern hemisphere was slightly higher than that on the southern hemisphere.
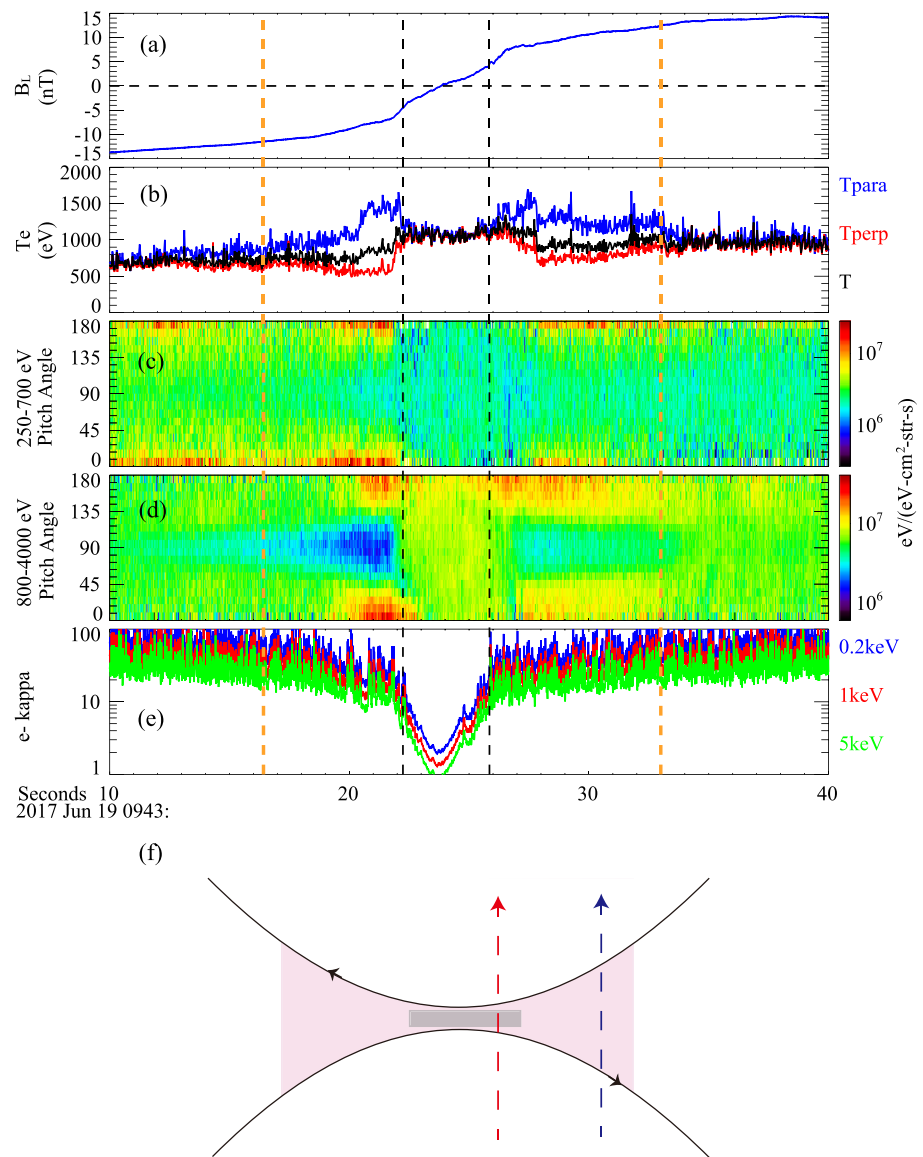
Figure 8. Electron temperature and pitch angle distributions (PADs) around the neutral sheet. (a) The magnetic field B_L; (b) electron parallel (blue), perpendicular (red), and average temperature (black); (c) electron PAD in the energy range of 250–700 eV and (d) 800–4,000 eV; and (e) electron adiabatic parameter κ for three different energies: 0.2 keV (blue), 1 keV (red), and 5 keV (green). The two orange dashed lines mark the locations of $|B_L| = 12$ nT, while the two black dashed lines mark the boundaries of the isotropic electrons. Panel (f) schematizes the shape of the electron isotropic region. The two dashed lines in panel (f) denote the magnetospheric multiscale (MMS) trajectory across the diffusion region in the Aug10 event and this event, respectively.

Similar temperature anisotropy and bidirectional electron velocity distributions have been found in the inflow region of the diffusion region (Chen et al., 2009; Huang et al., 2018; Zhou et al., 2019). It is suggested that acceleration by parallel electric field causes the temperature anisotropy in the inflow region (Egedal et al., 2010). Figure 8e shows the electron adiabatic parameter κ for three different energies: 0.2, 1, and 5 keV, respectively. Here, κ is defined as the square root of the ratio between the local magnetic field curvature radius and the electron Larmor radius (Büchner & Zelenyi, 1989). The asymptotic κ values were above 20. They dropped significantly as they approach the neutral sheet. The sudden decrease of κ was nearly coincident with the disappearance of the temperature anisotropy. The minimum value of κ for electrons of 5 keV was less than 1 and was less than 3 for the 0.2-keV electrons. This means that electrons were mostly nonadiabatic and suffered pitch angle mixing/scattering. Therefore, the disappearance of anisotropy within the

IDR was probably caused by the pitch angle mixing/scattering due to the highly curved magnetic field lines, which has been demonstrated to cause the isotropic and gyrotropic electron distributions in the EDR (Lavraud et al., 2016; Zhou et al., 2019).

5. Discussion and Summary

One possible reason accounting for these asymmetries is that they were the consequence of the oblique trajectory of MMS across the IDR, which is discussed in section 3. Knowing the motion speed of the X-line in **L**, we evaluated the horizontal distance between the two crosspoints of the MMS trajectory and the separatrices, which was about 0.4 d_i. If the observed asymmetries were due to the different location in **L**, it indicates that the IDR is not uniform on the sub-ion scale. On the other hand, it is suggested that X-line is the antinode/maximum of E_N from superposition of two antipropagating kinetic Alfven wave mode (Dai, 2009). Hence, MMS is expected to observe larger E_N closer to the X-line, which is consistent with our observations.

An alternative explanation is that they were caused by the guide field. It has been shown that guide field breaks the symmetry of Hall magnetic and electric field (Eastwood, Shay, et al., 2010; Zhou, Deng, et al., 2014; Zhou et al., 2018) because the imposed guide field B_M induces a Lorentz force $J_L \times B_M$ that deflects the Hall current in the reconnecting plane. Fu et al. (2018) reported the tripolar E_N across the neutral sheet in guide field reconnection by particle simulation. However, the origin of the positive E_N on the northern hemisphere is inconsistent with our observation (see the discussion in section 4). We should note that the guide field was quite small (~0.1 B_0) in this IDR. A simulation with guide field of 10% of the asymptotic magnetic field in Fu et al. (2018) does not display the tripolar structure of E_N. In addition, they did not show the J·E′ and electron temperature in their simulations. Whether the observed asymmetries were due to the guide field or the oblique trajectory can be further investigated by kinetic simulations. We will address this issue in our future study.

MMS observed an EDR in the magnetotail on 10 August 2017 (Zhou et al., 2019). This EDR was embedded within a much larger IDR. A similar profile of electron temperature was observed in this event (we call it Aug10 event hereafter), that is, a temperature isotropic region was sandwiched by two regions with $T_\parallel > T_\perp$. It seems that this type of electron temperature profile is common in symmetric reconnection. Although the mechanism responsible for the isotropic distribution seems the same, the thicknesses of the electron isotropic region are quite different between the two cases. The thickness of the isotropic layer was 0.375 d_i ~ 16 d_e, which was much larger than the isotropic layer ~2 d_e on the Aug10 event. The isotropic region coincided well with the EDR in the Aug10 event, while the isotropic region observed in this event was inside the IDR but much broader than the EDR. The crossing of the neutral sheet occurred inside the EDR on the Aug10 event, probably a few d_e from the X line, while the crossing of the neutral sheet occurred at around 1.6 d_i from the X line in this event. Therefore, the thickness of the isotropic region increases as the horizontal distance with respect to the X line increases. We surmise that the boundary between the isotropic and anisotropic electrons has a shape similar to the separatrix with a large opening angle, as illustrated in Figure 8f.

In summary, MMS encountered a well-structured IDR in symmetric reconnection in the magnetotail. The reconnecting X line contained a small guide field of about 1.5 nT, nearly 10% of the asymptotic magnetic field. The main results are summarized as follows:

i The out-of-plane current J_M bifurcated in the IDR. It peaked at the boundary between the inflow and outflow electrons along the separatrix. The thicknesses of the peak J_M were a few d_e. Magnetic energy conversion and dissipation predominantly occurred at the peak of the out-of-plane current instead of at the neutral sheet center where $B_L = 0$.

ii Both the energy dissipation and normal electric field E_N exhibited evident asymmetry with respect to the neutral sheet. The energy dissipation was larger around the northern separatrix than around the southern separatrix. The electric field E_N showed a tripolar variation across the neutral sheet, that is, a unipolar E_N around the southern separatrix and a bipolar E_N around the northern separatrix. The positive E_N on the northern separatrix was an electron-scale structure and was caused by electron physics.

iii Electrons were anisotropic away from the neutral sheet and became isotropic within the neutral sheet. The isotropization of the electrons was likely caused by the pitch angle scattering in highly curved field lines at the center of the diffusion region. This isotropic region was substantially thicker than the

isotropic region in Aug10 event, during which MMS crossed the diffusion region much close to the X line. This implies that the thickness of the electron isotropic region strongly depends on the horizontal distance to the X line.

Our results reveal the sub-ion-scale structure and electron physics of the IDR in symmetric reconnection and will advance our understanding on the role of the IDR in reconnection.

References

Asano, Y., Mukai, T., Hoshino, M., Saito, Y., Hayakawa, H., & Nagai, T. (2003). Evolution of the thin current sheet in a substorm observed by Geotail[J]. *Journal of Geophysical Research*, *108*(A5), 1189. https://doi.org/10.1029/2002JA009785

Bessho, N., & Bhattacharjee, A. (2005). Collisionless reconnection in an electron-positron plasma. *Physical Review Letters*, *95*(24), 245001.

Birn, J., Drake, J. F., Shay, M. A., Rogers, B. N., Denton, R. E., Hesse, M., et al. (2001). Geospace environmental modeling (GEM) magnetic reconnection challenge. *Journal of Geophysical Research*, *106*(A3), 3715–3719.

Borg, A. L., Øieroset, M., Phan, T. D., Mozer, F. S., Pedersen, A., Mouikis, C., et al. (2005). Cluster encounter of a magnetic reconnection diffusion region in the near-Earth magnetotail on September 19, 2003[J]. *Geophysical Research Letters*, *32*(19), L19105. https://doi.org/10.1029/2005GL023794

Büchner, J., & Zelenyi, L. M. (1989). Regular and chaotic charged particle motion in magnetotail like field reversals: 1. Basic theory of trapped motion. *Journal of Geophysical Research*, *94*(A9), 11,821–11,842. https://doi.org/10.1029/JA094iA09p11821

Chaston, C. C., Phan, T. D., Bonnell, J. W., Mozer, F. S., Acuña, M., Goldstein, M. L., et al. (2005). Drift-kinetic Alfvén waves observed near a reconnection X line in the Earth's magnetopause[J]. *Physical Review Letters*, *95*(6), 065002.

Chen, L.-J., Bhattacharjee, A., Puhl-Quinn, P. A., Yang, H., Bessho, N., Imada, S., et al. (2008). Observation of energetic electrons within magnetic islands. *Nature Physics*, *4*, 19–23. https://doi.org/10.1038/nphys777

Dai, L. (2009). Collisionless magnetic reconnection via Alfvén eigenmodes. *Physical Review Letters*, *102*(245003). https://doi.org/10.1103/PhysRevLett.102.245003

Dai, L. (2018). Structures of Hall fields in asymmetric magnetic reconnection. *Journal of Geophysical Research: Space Physics*, *123*, 7332–7341. https://doi.org/10.1029/2018JA025251

Dai, L., Wang, C., Angelopoulos, V., & Glassmeier, K.-H. (2015). In situ evidence of breaking the ion frozen-in condition via the non-gyrotropic pressure effect in magnetic reconnection. *Annales Geophysicae*, *33*, 1147–1153. https://doi.org/10.5194/angeo-33-1147-2015

Dai, L., Wang, C., Zhang, Y., Lavraud, B., Burch, J., Pollock, C., & Torbert, R. B. (2017). Kinetic Alfvén wave explanation of the Hall fields in magnetic reconnection[J]. *Geophysical Research Letters*, *44*, 634–640.

Deng, X. H., & Matsumoto, H. (2001). Rapid magnetic reconnection in the Earth's magnetosphere mediated by whistler waves[J]. *Nature*, *410*(6828), 557.

Eastwood, J. P., Phan, T. D., Mozer, F. S., Shay, M. A., Fujimoto, M., Retino, A., et al. (2007). Multi-point observations of the Hall electromagnetic field and secondary island formation during magnetic reconnection. *Journal of Geophysical Research*, *112*(A6), A06235. https://doi.org/10.1029/2006JA012158

Eastwood, J. P., Phan, T. D., Øieroset, M., & Shay, M. A. (2010). Average properties of the magnetic reconnection ion diffusion region in the Earth's magnetotail: The 2001–2005 Cluster observations and comparison with simulations. *Journal of Geophysical Research*, *115*(A8), A08215. https://doi.org/10.1029/2009JA014962

Eastwood, J. P., Shay, M. A., Phan, T. D., & Øieroset, M. (2010). Asymmetry of the ion diffusion region Hall electric and magnetic fields during guide field reconnection: Observations and comparison with simulations[J]. *Physical Review Letters*, *104*(20), 205001.

Egedal, J., Lê, A., Katz, N., Chen, L.-J., Lefebvre, B., Daughton, W., & Fazakerley, A. (2010). Cluster observations of bidirectional beams caused by electron trapping during antiparallel reconnection. *Journal of Geophysical Research*, *115*, A03214. https://doi.org/10.1029/2009JA014650

Ergun, R. E., Tucker, S., Westfall, J., et al. (2016). The axial double probe and fields signal processing for the MMS mission[J]. *Space Science Reviews*, *199*(1-4), 167–188.

Fu, H. S., Cao, J. B., Khotyaintsev, Y. V., et al. (2013). Dipolarization fronts as a consequence of transient reconnection: In situ evidence[J]. *Geophysical Research Letters*, *40*, 6023–6027.

Fu, S., Huang, S., Zhou, M., et al. (2018). Tripolar electric field structure in guide field magnetic reconnection[C]//Annales Geophysicae. *Copernicus GmbH*, *36*(2), 373–379.

Graham, D. B., Khotyaintsev, Y. V., Norgren, C., et al. (2016). Electron currents and heating in the ion diffusion region of asymmetric reconnection[J]. *Geophysical Research Letters*, *43*, 4691–4700.

Huang, S. Y., Fu, H. S., Yuan, Z. G., Vaivads, A., Khotyaintsev, Y. V., Retino, A., et al. (2016). Two types of whistler waves in the hall reconnection region[J]. *Journal of Geophysical Research: Space Physics*, *121*, 6639–6646.

Huang, S. Y., K. Jiang, Z. G. Yuan et al. (2018). Observations of the electron jet generated by secondary reconnection in the magnetotail, *The Astrophysical Journal*, *862*, 144. https://doi.org/10.3847/1538-4357/aacd4c

Huang, S. Y., Vaivads, A., Khotyaintsev, Y. V., Zhou, M., Fu, H. S., Retinò, A., et al. (2012). Electron acceleration in the reconnection diffusion region: Cluster observations[J]. *Geophysical Research Letters*, *39*(11), L11103. https://doi.org/10.1029/2012GL051946

Huang, S. Y., Yuan, Z. G., Sahraoui, F., Fu, H. S., Pang, Y., Zhou, M., et al. (2017). Occurrence rate of whistler waves in the magnetotail reconnection region. *Journal of Geophysical Research: Space Physics*, *122*, 7188–7196. https://doi.org/10.1002/2016JA023670

Huang, S. Y., Zhou, M., Sahraoui, F., Deng, X. H., Pang, Y., Yuan, Z. G., et al. (2010). Wave properties in the magnetic reconnection diffusion region with high b: Application of the k-filtering method to Cluster multispacecraft data. *Journal of Geophysical Research*, *115*, A12211. https://doi.org/10.1029/2010JA015335

Lavraud, B., Zhang, Y. C., Vernisse, Y., Gershman, D. J., Dorelli, J., Cassak, P. A., et al. (2016). Currents and associated electron scattering and bouncing near the diffusion region at Earth's magnetopause. *Geophysical Research Letters*, *43*, 3042–3050. https://doi.org/10.1002/2016GL068359

Lindqvist, P. A., Olsson, G., Torbert, R. B., et al. (2016). The spin-plane double probe electric field instrument for MMS[J]. *Space Science Reviews*, *199*(1-4), 137–165.

Liu, Y. H., Hesse, M., Guo, F., Daughton, W., Li, H., Cassak, P. A., & Shay, M. A. (2017). Why does steady-state magnetic reconnection have a maximum local rate of order 0.1?[J]. *Physical Review Letters*, *118*(8), 085101.

Lu, Q., Huang, C., Xie, J., et al. (2010). Features of separatrix regions in magnetic reconnection: Comparison of 2-D particle-in-cell simulations and Cluster observations[J]. *Journal of Geophysical Research*, *115*(A11), A11208. https://doi.org/10.1029/2010JA015713

Mozer, F. S., Pritchett, P. L., Bonnell, J., Sundkvist, D., & Chang, M. T. (2008). Observations and simulations of asymmetric magnetic field reconnection. *Journal of Geophysical Research*, *113*, A00C03. https://doi.org/10.1029/2008JA013535

Nagai, T., Shinohara, I., Fujimoto, M., Matsuoka, A., Saito, Y., & Mukai, T. (2011). Construction of magnetic reconnection in the near-Earth magnetotail with Geotail. *Journal of Geophysical Research*, *116*, A04222. https://doi.org/10.1029/2010JA016283

Nakamura, R., Baumjohann, W., Asano, Y., Runov, A., Balogh, A., Owen, C. J., et al. (2006). Dynamics of thin current sheets associated with magnetotail reconnection[J]. *Journal of Geophysical Research*, *111*(A11), A11206. https://doi.org/10.1029/2006JA011706

Øieroset, M., Phan, T. D., Fujimoto, M., Lin, R. P., & Lepping, R. P. (2001). In situ detection of collisionless reconnection in the Earth's magnetotail[J]. *Nature*, *412*(6845), 414.

Phan, T. D., Eastwood, J. P., Cassak, P. A., Øieroset, M., Gosling, J. T., Gershman, D. J., et al. (2016). MMS observations of electron-scale filamentary currents in the reconnection exhaust and near the X line. *Geophysical Research Letters*, *43*, 6060–6069. https://doi.org/10.1002/2016GL069212

Pollock, C., Moore, T., Jacques, A., et al. (2016). Fast plasma investigation for magnetospheric multiscale[J]. *Space Science Reviews*, *199*(1-4), 331–406.

Pritchett, P. L. (2001). Geospace environment modeling magnetic reconnection challenge: Simulations with a full particle electromagnetic code[J]. *Journal of Geophysical Research*, *106*(A3), 3783–3798.

Robert, P., & Roux, A. (1993). Influence of the shape of the tetrahedron on the accuracy of the estimate of the current density. In *Proceedings of ESA 'START' Conference, Aussois, France, Centre de Recherches en Physique de l'Environment*. Issy les: Moulineaux, France; ESA WPP-047, 289–293.

Runov, A., Nakamura, R., Baumjohann, W., et al. (2003). Current sheet structure near magnetic X-line observed by Cluster[J]. *Geophysical Research Letters*, *30*(11), 1579. https://doi.org/10.1029/2002GL016730

Russell, C. T., Anderson, B. J., Baumjohann, W., et al. (2016). The magnetospheric multiscale magnetometers[J]. *Space Science Reviews*, *199*(1-4), 189–256.

Sharma, A. S., Nakamura, R., Runov, A., Grigorenko, E. E., Hasegawa, H., Hoshino, M., et al. (2008). Transient and localized processes in the magnetotail: A review. *Annales de Geophysique*, *26*, 955–1006.

Sonnerup, B. U. O., & Scheible, M. (1998). Minimum and maximum variance analysis, Chap. 1. In G. Paschmann, & P. W. Daly (Eds.), *Analysis methods for multi-spacecraft data, No. SR-001 in ISSI Scientific Reports* (pp. 185–220). Noordwijk, Netherlands: ESA Publications Division.

Tanaka, K. G., Retinò, A., Asano, Y., Fujimoto, M., Shinohara, I., Vaivads, A., et al. (2008). Effects on magnetic reconnection of a density asymmetry across the current sheet. *Annales Geophysicae*, *26*, 2471–2483. https://doi.org/10.5194/angeo-26-2471-2008

Teh, W. L., Eriksson, S., Sonnerup, B. U. Ö., et al. (2010). THEMIS observations of a secondary magnetic island within the Hall electromagnetic field region at the magnetopause[J]. *Geophysical Research Letters*, *37*(21), L21102. https://doi.org/10.1029/2010GL045056

Torbert, R. B., Burch, J. L., Phan, T. D., et al. (2018). Electron-scale dynamics of the diffusion region during symmetric magnetic reconnection in space[J]. *Science*, *362*(6421), 1391–1395.

Viberg, H., Khotyaintsev, Y. V., Vaivads, A., et al. (2013). Mapping HF waves in the reconnection diffusion region[J]. *Geophysical Research Letters*, *40*, 1032–1037.

Wang, R., Lu, Q., Du, A., et al. (2010). In situ observations of a secondary magnetic island in an ion diffusion region and associated energetic electrons[J]. *Physical Review Letters*, *104*(17), 175003.

Wang, R., Nakamura, R., Lu, Q., et al. (2012). Asymmetry in the current sheet and secondary magnetic flux ropes during guide field magnetic reconnection[J]. *Journal of Geophysical Research: Space Physics*, *117*(A7).

Wang, S., Chen, L. J., Hesse, M., et al. (2016). Ion demagnetization in the magnetopause current layer observed by MMS[J]. *Geophysical Research Letters*, *43*(10), 4850–4857.

Wygant, J. R., Cattell, C. A., Lysak, R., Song, Y., Dombeck, J., McFadden, J., et al. (2005). Cluster observations of an intense normal component of the electric field at a thin reconnecting current sheet in the tail and its role in the shock-like acceleration of the ion fluid into the separatrix region. *Journal of Geophysical Research*, *110*, A09206. https://doi.org/10.1029/2004JA010708

Zhang, Y., Lavraud, B., Dai, L., Wang, C., Marchaudon, A., Avanov, L., et al. (2017). Quantitative analysis of a Hall system in the exhaust of asymmetric magnetic reconnection. *Journal of Geophysical Research: Space Physics*, *122*, 5277–5289. https://doi.org/10.1002/2016JA023620

Zhou, M., Ashour-Abdalla, M., Berchem, J., et al. (2016). Observation of high-frequency electrostatic waves in the vicinity of the reconnection ion diffusion region by the spacecraft of the Magnetospheric Multiscale (MMS) mission[J]. *Geophysical Research Letters*, *43*(10), 4808–4815.

Zhou, M., Ashour-Abdalla, M., Deng, X., Pang, Y., Fu, H., Walker, R., et al. (2017). Observation of three-dimensional magnetic reconnection in the terrestrial magnetotail. *Journal of Geophysical Research: Space Physics*, *122*(9), 9513–9520.

Zhou, M., Berchem, J., Walker, R. J., El-Alaoui, M., Goldstein, M. L., Lapenta, G., et al. (2018). Magnetospheric Multiscale observations of an ion diffusion region with large guide field at the magnetopause: Current system, electron heating, and plasma waves. *Journal of Geophysical Research: Space Physics*, *123*. https://doi.org/10.1002/2017JA024517

Zhou, M., Deng, X., Tang, R., Pang, Y., Xu, X., Yuan, Z., & Huang, S. (2014). Evidence of deflected super-Alfvénic electron jet in a reconnection region with weak guide field[J]. *Journal of Geophysical Research: Space Physics*, *119*(3), 1541–1548.

Zhou, M., Deng, X. H., Li, S. Y., Pang, Y., Vaivads, A., Rème, H., et al. (2009). Observation of waves near lower hybrid frequency in the reconnection region with thin current sheet. *Journal of Geophysical Research: Space Physics*, *114*(A2).

Zhou, M., Deng, X. H., Pang, Y., et al. (2012). Revealing the sub-structures of the magnetic reconnection separatrix via particle-in-cell simulation[J]. *Physics of Plasmas*, *19*(7), 072907.

Zhou, M., Deng, X. H., Zhong, Z. H., Pang, Y., Tang, R. X., et al. (2019). Observations of an electron diffusion region in symmetric reconnection with weak guide field. *The Astrophysical Journal*, *870*, 34.

Zhou, M., Li, H., Deng, X., Huang, S., Pang, Y., Yuan, Z., et al. (2014). Characteristic distribution and possible roles of waves around the lower hybrid frequency in the magnetotail reconnection region[J]. *Journal of Geophysical Research: Space Physics*, *119*(10), 8228–8242.

Zhou, M., Pang, Y., Deng, X. H., Yuan, Z. G., & Huang, S. Y. (2011). Density cavity in magnetic reconnection diffusion region in the presence of guide field. *Journal of Geophysical Research: Space Physics*, *116*(A6).